1

The influence of surface roughness on the particle-pair distribution function of dilute suspensions of non-colloidal spheres in simple shear flow

By INDRESH RAMPALL †, JEFFREY R. SMART
AND DAVID T. LEIGHTON

Department of Chemical Engineering, University of Notre Dame, Notre Dame, IN 46556, USA

The pair distribution function of 3.18 mm diameter particles was measured in the plane of shear of a simple shear flow at concentrations of 5%, 10% and 15% by volume. A new direct flow-visualization procedure and a new pattern recognition algorithm were used in the investigation. The measurements show a depletion of bound pairs of particles in the direction of flow. A simple model which includes the effect of particle surface roughness on the particle interactions and the pair distribution function is presented. An important effect of surface roughness is that the particles in a suspension can experience irreversible interactions in the presence of an externally imposed simple shear flow. The model shows that such irreversibilities eliminate all bound pairs of particles in the plane of shear by displacing particles out of the closed orbit trajectory region. Surface roughness is found to induce significant asymmetry in the fore and aft region of a two-particle interaction. The measurements and predictions are in qualitative agreement with these conclusions.

---

1. Introduction

In this paper we examine the effect of the surface morphology of non-colloidal particles on the behaviour of sheared suspensions at low Reynolds numbers. One important property of a suspension is its effective viscosity: Einstein (1906) found that the effective viscosity of a dilute suspension of spheres is $\mu/\mu_0 = 1 + \frac{5}{2}c$, where μ is the effective suspension viscosity, μ_0 is the suspending fluid viscosity, and c is the volume fraction of suspended solids. Einstein's result is exact to $O(c)$ and is independent of the nature of particle interactions, which are significant at $O(c^2)$ in a dilute suspension. Surface roughness will have little influence on the coefficient $\frac{5}{2}$ in this result; if the roughness lengthscale $\epsilon_s a$ is small with respect to the particle radius a, then the increase in viscous dissipation owing to the roughness is at most $O(\epsilon_s)$ by the minimum dissipation theorem.

The constitutive equation for viscous dissipation can be extended to $O(c^2)$ by including the effect of two-particle interactions (Batchelor & Green 1972b). Particle interactions in a flowing suspension can lead to a non-uniform suspension microstructure. In this work we shall demonstrate that surface roughness affects particle interactions, thereby strongly influencing the local distribution of particles as

† Present address: Holtec International, 555 Lincoln Drive West, Marlton, NJ 08053, USA.

well. We consider here suspensions of non-colloidal particles in which Brownian motion is negligible; surface forces, such as van der Waals and electroviscous forces, are unimportant on the lengthscale of the particle diameter; and the Reynolds number is sufficiently low that inertial effects are likewise negligible. Despite these restrictions this class of suspensions contains many examples of interest, and represents the high-Péclet-number/low-Reynolds-number limit of more general classes of suspensions.

Theoretical predictions of suspension microstructure are largely limited to dilute suspensions, in which only two-particle interactions need be considered. The microstructure of a dilute suspension is most easily described by the pair-particle conditional probability distribution function $P(x_0+r|x_0)$; $P(x_0+r|x_0)\,\delta V$ is the probability of finding a particle centre in a volume element δV centred at x_0+r, given that there is a particle centre at x_0. For large r, the particle positions become statistically independent of the presence of the reference particle at x_0. In this asymptotic limit $P(x_0+r|x_0)$ is equal to the average number of particles per unit volume of suspension. The pair-particle conditional probability distribution function is usually normalized with this average particle density and is then referred to as the pair distribution function (PDF) $q(r)$.

Batchelor & Green (1972a) calculated the pair distribution function of a dilute suspension of spheres undergoing purely hydrodynamic interactions by following the relative motion of pairs of spheres in an arbitrary linear shear flow. The trajectories were followed by starting from infinity, where the PDF is equal to unity. The PDF along a trajectory is obtained by solving the associated conservation equation for $q(r)$. These authors demonstrated that the dilute pair distribution function is spherically symmetric in all regions in which the particle trajectories begin at infinity, and, surprisingly, is independent of the type of linear shear flow (e.g. simple shear, extensional flow, etc.). Of course, there is a region of closed trajectories in any planar shear flow with vorticity; the probability density function cannot be evaluated in this region from two-particle interactions alone. The PDF in this region of simple shear flow can only be determined if three-body interactions are taken into account or if some non-hydrodynamic force, such as Brownian motion or a repulsive electroviscous force, is introduced to eliminate the closed orbit trajectories.

Arp & Mason (1977) found that the surface roughness of the particles used in their experiments eliminated closed-orbit trajectories. They calculated that the minimum gap width between two bound smooth spheres on the limiting closed orbit trajectory is approximately 4×10^{-5} sphere radii. Smart & Leighton (1989) found that the effective hydrodynamic surface roughness of non-colloidal spheres typically used in viscometric measurements is $O(10^{-3})$ to $O(10^{-2})$ sphere radii. Since the surface roughness lengthscale determines the minimum distance between surfaces, roughness can eliminate all bound pairs of particles in the plane of shear of a simple shear flow by displacing particles outside the closed orbit trajectory region. Particles can re-enter this region only via three-body interactions, which are rare in a dilute suspension, so the PDF may be calculated everywhere in the plane of shear.

Husband & Gadala-Maria (1987) measured the PDF of dilute suspensions and found an excess of particles aligned in the direction of fluid motion, contrary to what would be expected from the preceding analysis. Their structure corresponds to a relative excess of bound pairs of particles, since doublets spend the majority of time aligned with the direction of motion. In numerical simulations of dilute suspensions with only hydrodynamic forces present (i.e. no repulsive forces, such as would arise from surface roughness), Bossis & Brady (1985) predicted an excess of particles in the closed orbit region, in agreement with Husband & Gadala-Maria (1987). A depletion
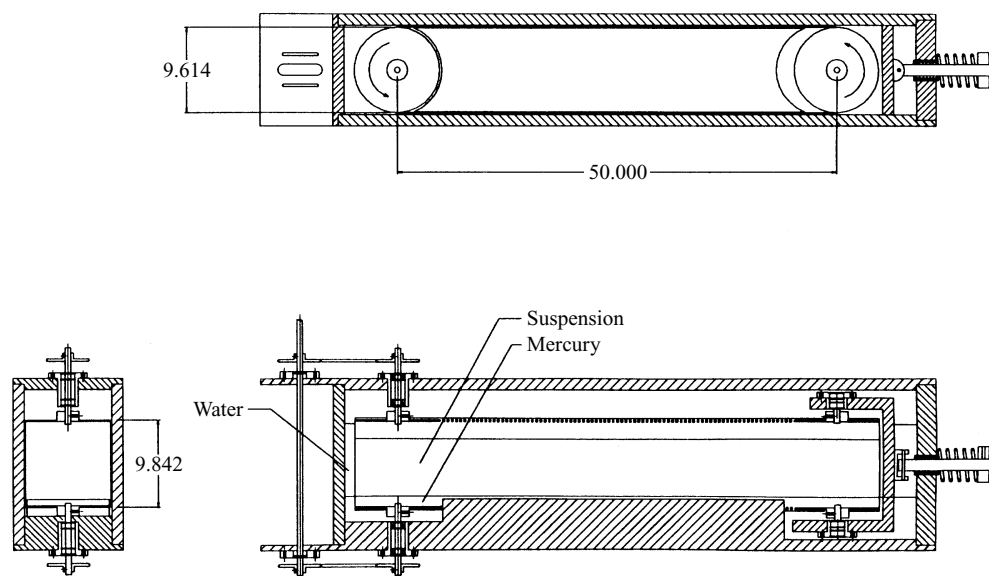
FIGURE 1. The shear tank experimental apparatus used in the flow-visualization experiments. The top view, side and end cross-sectional views are shown. The suspension was confined in the interior of a rotating film loop. Mercury provided a stress-free lower boundary. (All dimensions in cm.)

of particles in the closed orbit region was observed, however, when Bossis & Brady (1984) included strong interparticle repulsive forces in their numerical simulation. The discrepancy between the earlier experimental results and those expected for particles with significant surface roughness will be examined.

In the next section we describe a direct flow visualization technique used to measure the pair distribution function of a dilute suspension of spheres undergoing simple shear flow. A template matching technique used to obtain the locations of particle centres in digitized images is described in §3. Results obtained for 5%, 10% and 15% suspension experiments are presented in §4. The equations relating the true three-dimensional PDF and the two-dimensional PDF measured in the plane of shear are developed in §5. The effect of surface roughness on particle trajectories and the pair distribution function in the plane of shear of simple shear flow for a monodisperse suspension of spheres is investigated in §6 and compared to the experimental measurements. The conclusions are presented in the final section.

2. Laser sheet imaging

We have developed an imaging procedure in which the interior of a flowing suspension is illuminated with a thin horizontal sheet of laser light. This direct flow visualization procedure is related to earlier direct measurements of the microstructure of suspensions (Karnis, Goldsmith & Mason 1966; Graham & Bird 1984; Parsi & Gadala-Maria 1987); Leighton & Rampall (1992) reviewed these techniques and their limitations. In this work a monodisperse suspension of 3.18 mm diameter ground polymethylmethacrylate (PMMA) spheres suspended in a mixture of Triton X-100 (77 wt%), zinc chloride (13.8 wt%) and water (9.2 wt%) was prepared for flow visualization studies. The suspending fluid had a viscosity of 53 P and a density of 1.18 g cm^{-3} at 22.5 °C. The suspending fluid was Newtonian and the composition was

carefully adjusted by trial and error to closely match both the refractive index and density of the acrylic spheres. A small quantity of concentrated hydrochloric acid (approximately 0.03 wt %) was added to the solution to prevent the formation of zinc hypochlorite precipitate, thereby significantly improving the optical transparency of the solution. The suspension was largely transparent to the laser sheet owing to the careful matching of the index of refraction of the fluid and particles, but a small amount of light scattering occurred at the particle surfaces owing to either surface imperfections or a slight mismatch of the refractive index. Since the laser sheet was significantly thinner than the particle radius (approximately 0.5 mm *vs.* 3.18 mm), the surface scattering appeared as a plane of bright circles when viewed normal to the plane of the laser sheet. The centres of the circles corresponded to the projection of sphere centres onto the plane of the laser light. Thus, it was possible to construct a two-dimensional pair distribution function from single images, while the two-dimensional velocity profile can be generated from successive images.

Experiments were conducted with suspension concentrations of 5 %, 10 % and 15 % by volume. The suspensions were confined inside a belt (110 mm photographic film from which the emulsion had been stripped) in the shear tank depicted in figure 1. The shear tank was constructed with 10 mm thick transparent acrylic. A d.c. stepping motor drove the belt through a system of gears arranged so that no part of the drive system (except the belt itself) was in contact with the suspension. A layer of mercury provided a stress-free lower boundary. While the depth of this layer varied, it was at least 5 mm thick over the entire suspension. A measured amount of suspending fluid was slowly poured into the region bounded by the belt, then measured amounts of particles were added to the fluid, forming a suspension of known concentration and volume. The suspension, confined by the belt, thus filled a rectangular region 50 cm long by 9.6 cm wide together with 4.8 cm radius cylindrical ends to a depth of 7 cm. Approximately 3800 cm^{-3} of suspension were required to fill the shear tank up to this depth.

The suspension was sheared for many hours before starting any experiments. A thin layer of water between the shearing belt and the walls of the shear tank provided a lubricating layer for smooth motion of the belt. The applied shear rate was typically 0.5 s^{-1}, yielding a particle Reynolds number $\dot{\gamma}a^2\rho/\mu_0$ of 2×10^{-4}, where $\dot{\gamma}$ is the shear rate and ρ is the fluid density. The Péclet number $\dot{\gamma}\mu_0 a^3/(kT)$ was 2.6×10^{12} (where k is the Boltzmann constant and T the absolute temperature of the fluid), ensuring that Brownian effects were likewise negligible.

A 5 W Argon-ion laser and a combination of cylindrical and convex lenses produced the laser sheet used to illuminate the plane of shear. Figure 2 shows the field of view, the location of the laser sheet, and the camera orientation. The particles, which appeared as bright circles moving in the laser sheet, were videotaped for later processing. A typical digitized image of a 15 % suspension is shown in figure 3. Note the elliptical appearance of the bright circles resulting from non-square shaped pixels of the digitizing board. The velocity field in the central region of the device was $U_x = \dot{\gamma}y$, $U_y = U_z = 0$, where the x is the direction of flow, y is normal to the flow in the plane of shear, and z is the direction of gravity.

The laser sheet was approximately 2 cm below the top surface of the suspension and the camera was about 80 cm above the suspension. The shear tank was mounted on an XYZ table so the shear tank could be moved without disturbing the laser or the camera. The dimensions of the viewing window were measured by videotaping rulers in air placed at the level of the laser sheet. The depth of the laser sheet in the suspension
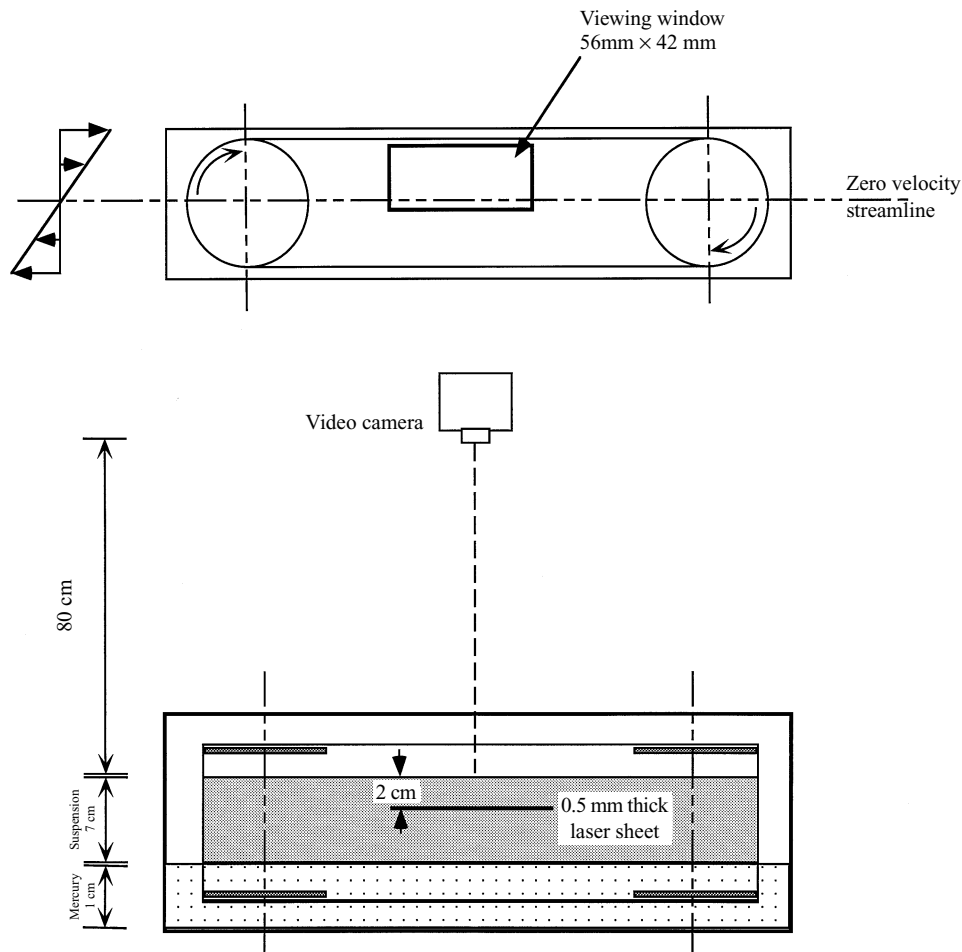
FIGURE 2. The flow-visualization experimental set-up showing the viewing window from the top of the shear tank. A cross-sectional side view schematically shows the location of the laser sheet, the orientation of the video camera, and the mercury and suspension levels.

was small compared to the distance from the laser sheet to the camera, thus the correction in the length calibration owing to the difference between the refractive index of the fluid and air was less than 1%.

The window of observation in the plane of the laser sheet was 5.6 cm (17.8 particle diameters) in the flow direction and 4.2 cm (13.4 particle diameters) normal to the flow direction. The window was approximately 1 cm (3 particle diameters) away from the shearing belt and included the zero velocity streamline. The viewing window was approximately centred in the direction of flow from the ends of the device. The flow observed in the viewing window was expected to be close to simple shear flow since disturbances from the ends decay exponentially over a lengthscale which is a fraction of the shear tank width. Note that particles close to the zero velocity streamline spend more time in the viewing window than do the faster moving particles near the walls.
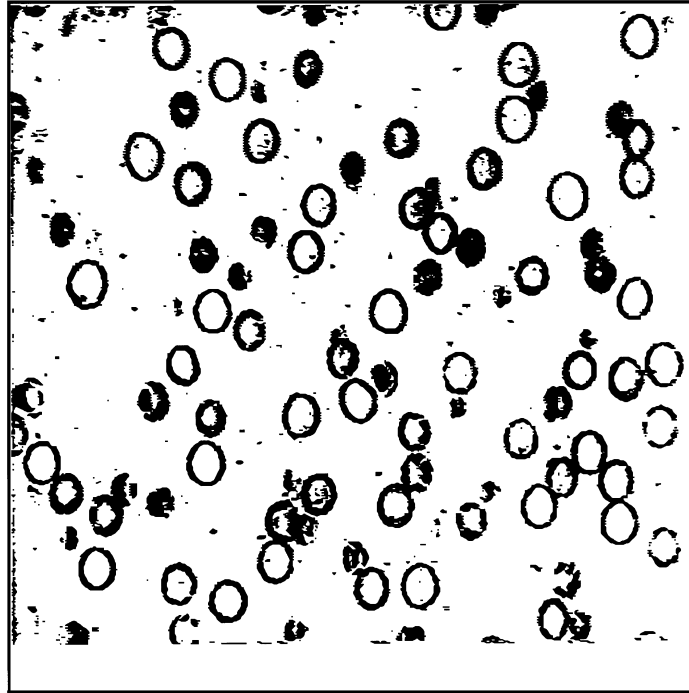
FIGURE 3. Cross-section of a digitized video frame for a 15% suspension of 3.18 mm acrylic spheres in the plane of shear. Note that the spheres appear as ellipses elongated in the vertical direction. This is due to the aspect ratio of the pixels in the digitized frame being equal to 0.8. The apparent radius of the spheres in the digitized image is 15.6 pixels vertically and 12.5 pixels horizontally.
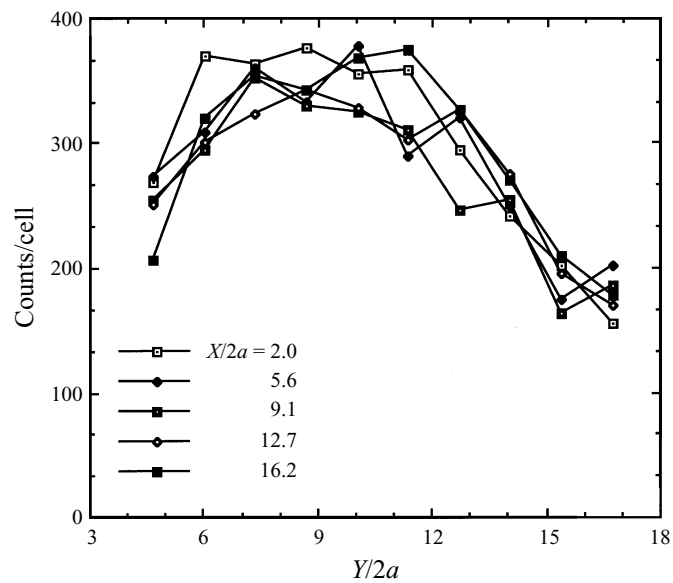

FIGURE 4. The number of particle centres per cell *vs.* distance from the wall for the 5% suspension. Note the sharp depletion in average particle concentration near the zero velocity streamline and near the wall.

3. Extension of matched filtering techniques for analysis of digitized images

The centre locations and radii of the bright circles in each image must be determined accurately to acquire useful information from the videotapes. Conventional template matching techniques useful for detecting patterns in noisy signals can only identify the positions of objects of a uniform size and shape (Rosenfeld & Kak 1982). In this flow-visualization procedure, the video images contain circles of differing radii because the sphere centres were not always in the plane of the laser sheet. We extended match filtering techniques to overcome this difficulty. The approach employed here uses FFT routines to convolve the digitized images containing the circles with the image of a complex disk. The radius of the disk is that of the largest circle in the original image, with unit modulus, but its phase varies radially so the disk contains equal areas of all phases. This mask is given by:

$$
M = \begin{cases} \exp\left(\dfrac{2\pi i r^2}{a^2}\right) & (r \leqslant a), \\ 0 & (r \geqslant a), \end{cases}
\tag{3.1}
$$

where a is the radius of the largest circle and $i = (-1)^{1/2}$. The convolution of this mask with an image containing bright circles results in a local maximum at the centre of each circle; the size r_c of circles in the original image may be calculated from the phase of this local maximum θ_c:

$$
\frac{r_c}{a} = \left(\frac{\theta_c}{2\pi}\right)^{1/2}.
\tag{3.2}
$$

Obtaining both the location and size of the bright circles in the digitized images can be understood in terms of the constructive interference of the pixels at the perimeter of each bright circle with the mask when the complex filter is directly centred on a circle during the convolution operation. We increased the accuracy of locating the sphere centres by examining the intensity of pixels near the centre of each bright circle in the convolved image space. A quadratic relation was fitted through three points in each direction; the location of the maximum of this quadratic function gives the best estimate of the location of the true centre of each circle.

The algorithm we developed to locate the centres of circles in the images is susceptible to two types of error. First, random noise in the digitized images and neighbouring bright circles affected the calculated location of centres of bright circles. Secondly, the procedure occasionally generated false positives at a lower magnitude (in the convolved image space) than the bright circles actually present in the digitized image. The second source of error, caused by partial constructive interference when the mask is between neighbouring bright circles, is unavoidable. However, such spurious identifications can be spotted and removed from the list of particles during the subsequent processing steps described in the following paragraphs.

We tracked the position of a bright circle in ten consecutive video frames in a 5% suspension to estimate the error in locating the centre of bright circles owing to random noise. Since the total elapsed strain during this time interval was small (about 0.16), the motion of the sphere should be steady, which was confirmed by fitting a line to the data. The error in the best-fit line, about 0.1 pixel (the particle moved over 40 pixels), is an estimate of the error in locating the centres of bright circles. The error resulting from the presence of a neighbouring bright circle was calculated by applying the

algorithm to a simulated image which contained two touching circles whose radii were 20 pixels and a mask radius of 25 pixels. The calculated location of one circle was shifted by approximately half a pixel toward the centre of the other circle.

The second source of error, that due to spurious identifications (i.e. finding particles that do not actually exist), was reduced considerably by retaining only those circles whose radius was larger than some chosen percentage of the particle radius a. The radius of most false positives was much smaller than the sphere radius; rejecting all circles with a radius less than $0.6a$ eliminated most of them. Eighty per cent of the spheres which can be illuminated by a laser sheet of negligible thickness (i.e. in a region of thickness $\pm a$ from the plane of the laser sheet) have a radius of at least $0.6a$. The list of particles is further scanned for inconsistencies, such as if the centre to centre spacing of any pair is less than the sum of their *apparent* radii. When two circles appear to intersect, which is physically impossible, the one with lower intensity is removed from the list. The intensity of each sphere centre is also compared to the intensity of the neighbouring circles. All circles whose intensity was less than 80% of the local average intensity were removed from the list of sphere centres in each processed image. These steps reduced the errors to within acceptable limits. To obtain an upperbound estimate of the false positive error rate, a randomly selected sample of the original and processed images were manually compared. The maximum number of false positives was two in an image containing approximately 30 particles, however, the majority of images sampled contained no false positives. The average false positive rate was approximately 0.02 per particle identified. The manual inspection procedure also showed that the loss rate (i.e. failure to identify particles actually present in the image) was negligible. Rampall (1992) has described the matched filtering technique in more detail.

4. Results

Approximately 1000 images for each of the 5%, 10% and 15% suspension experiments in simple shear flow were reduced to a list of sphere centre coordinates. The images of the suspensions were obtained from the central region of the shear tank apparatus, shown in figure 2. An apparent PDF in the plane of shear was generated by placing the origin of the coordinate system at the centre of each bright circle and counting the presence of the projection of other sphere centres into various cells defined in (r, θ) coordinate space [where $r = (x^2 + y^2)^{1/2}$ and $\theta = \tan^{-1}(y/x)$]. Far from the walls, the pair distribution function of a homogeneous suspension is symmetric about the origin (i.e. $g(r, \theta) = g(r, \theta + \pi)$). In a finite-size device, concentration inhomogeneities and wall effects will influence the PDF. These effects were reduced in our analysis by averaging $g(r, \theta)$ with its reflection through the origin. Hence, only the variation from 0 to π was accounted for by dividing the θ-space into 10 segments over the range $0°$ to $180°$. The extensional quadrant of the imposed shear flow is thus in the $0° < \theta < 90°$ range while the approach quadrant is in the $90° < \theta < 180°$ range. The radial space was divided into 64 segments over the range 0 to 5 sphere radii while the angular space was divided into 10 equally spaced $18°$ wedges.

The viewing window shown in figure 2 was divided into rectangular cells to estimate the magnitude of concentration inhomogeneities in the shear tank. The length and width of the viewing window were both divided into 10 segments. The number of bright circles in each cell was obtained from the list of sphere centre coordinates. In general, statistically significant concentration inhomogeneities normal to the flow direction were observed, while concentration in the flow direction was uniform. In figure 4 the
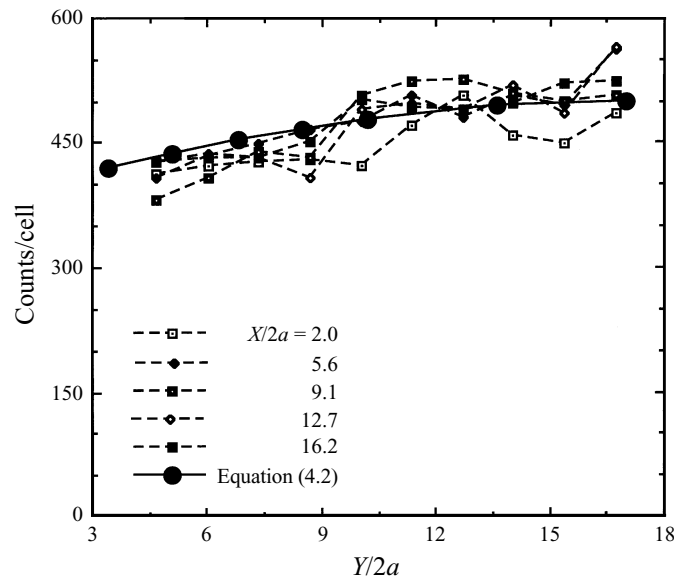
FIGURE 5. The number of particle centres per cell *vs.* distance from the wall for the 10% suspension. Note the small increase in average particle density from the near wall region to the zero velocity streamline.

number of particle centres per cell is plotted as a function of the distance $Y/2a$ between each cell centre and the wall for the 5% suspension. This figure shows a sharp depletion of particles in the region $12 \leqslant Y/(2a) \leqslant 15$, which is near the zero velocity streamline and a smaller depletion near the wall. The apparent PDF for the 5% suspension was calculated from observations in a central region of the viewing window, where the particle concentration was essentially uniform. This window was rectangular with $6 < Y/(2a) < 12$ in the *y*-direction, and extended horizontally across the viewing window in the *x*-direction. Figure 5 shows the counts per cell for the 10% suspension experiments. The large variations in particle distribution found in the 5% suspensions are not observed here. However, there is a small systematic increase in concentration from the wall to the zero velocity streamline.

While the particles were slightly negatively buoyant (particles typically settled one diameter in approximately 10 min), they remained in suspension from top to bottom of the shear tank during shear for all of the experiments in this study. Despite the small sedimentation velocity, the shear-induced hydrodynamic diffusion mechanism for dispersing particles in a shear flow described by Leighton & Acrivos (1986, 1987) is insufficient to explain the resuspension at the lowest concentration examined here. At this concentration, shear induced dispersion is not only very weak but also requires a shearing time of the order of 40 h to approach steady state.

While the cause of the dependence of the concentration profile in the plane of shear observed in the 5% concentration experiments is unclear we surmise that the resuspension process in the vertical direction is due instead to the presence of weak secondary currents in the shear tank apparatus. A symmetric circulation pattern with downflow along the centreline and upflow at the walls would, in concert with the slow sedimentation velocity of the particles of similar magnitude, lead to the observed depletion at the centreline. Such a current would not be directly observable since the sedimentation velocity is some four orders of magnitude less than the imposed velocity

of the shearing belt. Note that while a secondary current may influence the bulk concentration distribution of the particles, it is unlikely to influence the local microstructure of principal interest here because of its small magnitude.

The concentration distribution observed for the 10 % suspension was more amenable to analysis. In this case shear-induced dispersion theory would require about 8 h of shearing to approach steady state, which is comparable to the duration of the experiments, and is sufficient to resuspend the particles. The difference in the 10 % concentrated suspension experiments from the 5 % concentration study arises from the strong dependence of the diffusivity on concentration (Leighton & Acrivos 1987). One possible explanation for the concentration inhomogeneity in the Y-direction is by postulating a balance between the inertial drift away from the walls predicted by Ho & Leal (1974) and shear-induced migration. While the dependence of the drift velocity on position in plane Couette flow is complex, it can be approximated by:

$$u_\xi \approx -16.8 \frac{\rho \dot{\gamma} a^3}{6\pi\mu_0} \left(\frac{\xi}{2b}\right), \tag{4.1}$$

where ξ is the distance from the zero velocity plane and $2b$ is the device width (the distance between shearing belts). The constant in equation (4.1) is obtained from a linear fit to the exact expression derived by Ho & Leal valid in the bulk of the flow (i.e. away from the walls). At steady state this drift velocity is balanced by a diffusive flux characterized by the shear-induced diffusivity in the plane of shear $D_\parallel$. Thus we obtain:

$$\frac{\mathrm{d}\phi}{\mathrm{d}\xi} \approx \frac{u_\xi \phi}{D_\parallel}, \tag{4.2}$$

where

$$\left.\begin{aligned} D_\parallel &= \hat{D}_\parallel \dot{\gamma} a^2 \\ &\approx \tfrac{1}{3}\phi^2(1+\tfrac{1}{2}\mathrm{e}^{8.8\phi})\,\dot{\gamma} a^2, \end{aligned}\right\} \tag{4.3}$$

where the dimensionless diffusivity $\hat{D}_\parallel$ in equation (4.3) is suggested by Leighton & Acrivos (1986). As may be seen from figure 5, a solution to (4.2) provides a good description of the observed concentration profile. While the degree of agreement is probably fortuitous, it does suggest that inertia plays an important role over large lengthscales at low concentrations, even for the low Reynolds numbers used in these experiments. We note that the concentration variation at an average suspension concentration of 15 % predicted from (4.2) is negligible (less than 1 %). This prediction again matches well with the experiments in which no discernible concentration variation was observed at 15 % suspension concentration.

An important consideration was whether sufficient strain had elapsed in the observation window for the PDF to approach its steady distribution. To investigate this, we divided the selected window into two non-overlapping regions. The first subregion was a thin horizontal rectangle enclosing the zero velocity axis, where the elapsed strain was expected to be large. The strain experienced by particles in the time taken for them to travel from one end of the shear tank into this viewing window was greater than 30. The second subregion was the uniform concentration region described above ($6 \leqslant Y/2a \leqslant 12$). The elapsed strain experienced by the particles in the second region was between 7.7 and 30. The PDF determined in each of these regions for the 10 % concentration suspension are compared in the next section.

In principle, the observation window must be infinitely large to calculate the PDF. In practice, however, the PDF must be estimated from information obtained in a finite
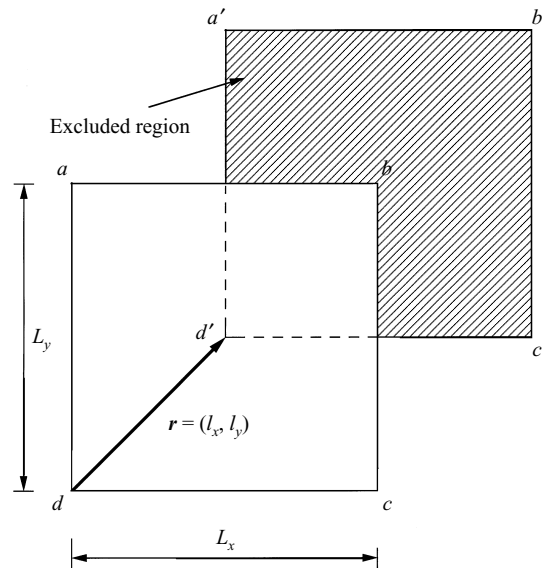
FIGURE 6. Finite-size window correction for calculating the pair distribution function. The region [*abcd*] is any chosen finite-sized observation window. The region [*a′b′c′d′*] corresponds to all possible positions which the end of any given displacement vector *r* will traverse for all possible reference particle positions within the chosen window. Note the excluded region which reduces the observed estimation of the true number of counts for this particular displacement vector.

window. The errors in estimating $q(\mathbf{r})$ are typically small for $r/L \ll 1$, where L is the characteristic window dimension, but become unbounded as $r/L \to 1$. These errors can be corrected if the window size is significantly larger than the maximum distance at which $q(\mathbf{r})$ is calculated. Let (a, b, c, d) be a finite-sized window as shown in figure 6. Also, let $\mathbf{r}$ be the displacement vector from the reference sphere centre 0 to the other sphere 1 under consideration. For suspensions with uniform concentration, sphere 0 is equally likely to be anywhere in the chosen window. For any displacement vector $\mathbf{r}$ there will be some pairs for which sphere 1 lies outside this observation window. This results in a reduced count of the number of observations for this particular displacement vector. The number of excluded observations becomes proportional to this excluded area as the number of observations becomes very large. Therefore, we may correct for this bias if the number of pairs observed for a particular $\mathbf{r}$ is increased by a factor of $L_x L_y/(L_x - l_x)/L_y - l_y)$ where L_x and L_y are the dimensions of the finite-sized window and l_x and l_y are the coordinates of the displacement vector $\mathbf{r}$.

The window dimensions for the 5% suspension were 17.8 particle diameters in the x-direction and 8.1 particle diameters in the y-direction. The PDF for $r/a < 5$ is estimated from the locations of sphere centres in this window. The maximum factor by which the counts in any cell will be increased is given by a displacement vector pointing parallel to the smaller dimension of the rectangular window. This correction factor is $8.1/(8.1 - 2.5) = 1.44$, which corresponds to a displacement vector counted in the outermost cell at the maximum distance of 5 radii from the origin at an angle of 90°. The correction to the PDF in the flow direction close to the origin ($r/a = 2$) is much smaller, only about 6%.

5. Deconvolution of the pair distribution function

The measured pair-particle probability distribution function is the probability of finding the projection of a sphere centre in an area $\rho \, d\rho \, d\theta$ of the projection plane, given that there is a projection of a sphere centre at the origin, where ρ is the radial coordinate in the plane of the laser sheet. However, since $q(\mathbf{r})$ is a three-dimensional function of the position vector $\mathbf{r}$, the measured pair-particle probability distribution function must be modified to account for this projection and to obtain the underlying three-dimensional PDF. Let $P_a(\mathbf{r})$ and $P(\rho, \theta)$ be the true and experimentally calculated pair-probability distribution functions, respectively. Then, from figure 7, the probability of finding sphere 1 in the plane of the laser sheet, given that sphere 0 is a distance b_0 from the plane of laser sheet, is:

$$P(\rho, \theta)\rho \, d\rho \, d\theta = \left\{ \int_{-b_0-b_{max}}^{-b_0+b_{max}} P_a(r, \theta, \phi) \, dz \right\} \rho \, d\rho \, d\theta, \tag{5.1}$$

where:

$$r^2 = z^2 + \rho^2, \quad \phi = \tan^{-1}(z/\rho), \quad z = b_1 - b_0. \tag{5.2}$$

The parameter b_{max} is the maximum distance between a sphere centre included in the list of particles and the plane of laser light. All particles smaller than $0.6a$ are rejected during the image processing step described earlier, so b_{max} is $0.8a$.

In a homogeneous suspension, sphere 0 has an equal probability of being anywhere in the range $|b_0| \leqslant b_{max}$, so the relationship between the observed and actual distribution is:

$$P(\rho, \theta) = \frac{1}{2b_{max}} \int_{-b_{max}}^{b_{max}} \int_{-b-b_{max}}^{-b+b_{max}} P_a(r, \theta, \phi) \, dz \, db. \tag{5.3}$$

The integral identity

$$\int_{-a}^{a} \int_{-y-a}^{-y+a} f(z) \, dz \, dy = \int_{-2a}^{2a} (2a - |z|) f(z) \, dz \tag{5.4}$$

can be used to simplify equation (5.3):

$$P(\rho, \theta) = \frac{1}{2b_{max}} \int_{-2b_{max}}^{2b_{max}} (2b_{max} - |z|) \, P_a(r, \theta, \phi) \, dz. \tag{5.5}$$

We now assume that the variation of $P_a(r, \theta, \phi)$ with ϕ in the range $|\phi| < \tan^{-1}(2b_{max}/\rho)$ is negligible for simple shear flow. This approximation is reasonable since all the spheres used in constructing the PDF are close to the plane of shear and $\partial P_a/\partial \phi = 0$ in this plane by symmetry. Transforming to a new set of variables $t = \rho^2$ and $\tau = r^2 = \rho^2 + z^2$, the following integral equation is obtained:

$$P(t, \theta) = \int_{t}^{t+4b_{max}^2} \left[\frac{1}{(\tau - t)^{1/2}} - \frac{1}{2b_{max}} \right] P_a(\tau, \theta) \, d\tau. \tag{5.6}$$

Equation (5.6) can be rewritten as a convolution integral in terms of an auxiliary function $G(t)$, which has an integrable singularity at the origin:

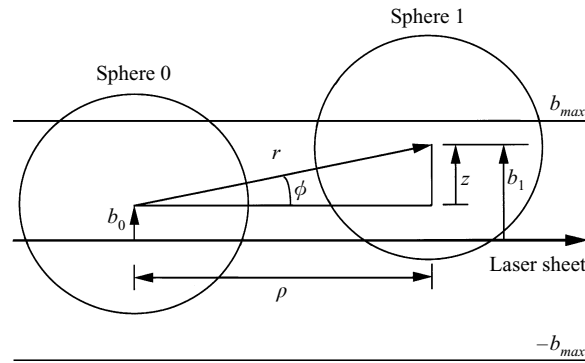$$P(t, \theta) = \int_{-\infty}^{\infty} G(t - \tau) \, P_a(\tau, \theta) \, d\tau, \tag{5.7}$$

FIGURE 7. Relationship between the observed pair distribution and the true pair distribution function; b is the distance out of the centre of the plane of the laser sheet. Only spheres whose centres are within $|b| < b_{max}$ are used to construct the pair distribution function.
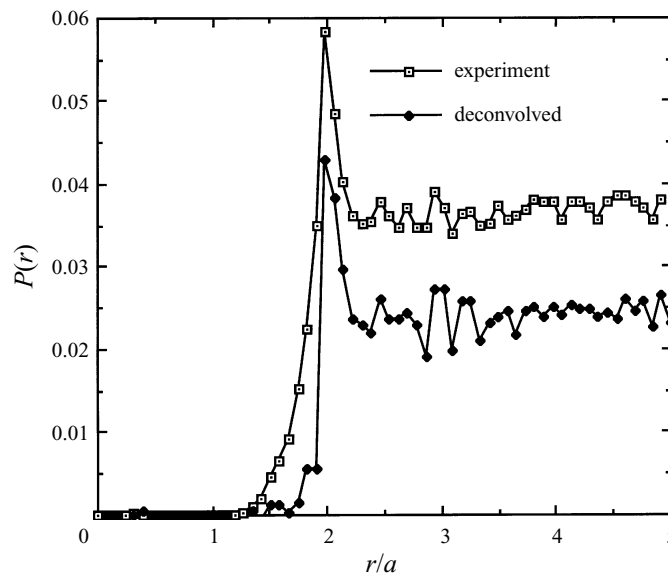

FIGURE 8. Deconvolution of the radial pair distribution function for 10% suspension. Data for the pair distribution function are averaged over all angles in the plane of shear. The deconvolved pair distribution function has a sharp singularity at $r/a = 2$ and a significant reduction in the forbidden region $r/a < 2$.

where the convolution kernel $G(t)$ is:

$$G(t) = \begin{cases} 0 & (t < -4b_{max}^2), \\ \dfrac{1}{(-t)^{1/2}} - \dfrac{1}{2b_{max}} & (-4b_{max}^2 < t < 0), \\ 0 & (t > 0). \end{cases} \tag{5.8}$$

The function $P(t, \theta)$ is the experimentally measured pair-particle probability density function at discrete radial and angular positions in the plane of shear. The function $P_a(\tau, \theta)$ is the true pair-particle probability density function in the plane of shear, and is formulated as an inverse convolution problem. Equation (5.7) is solved for $P_a(\tau, \theta)$ at
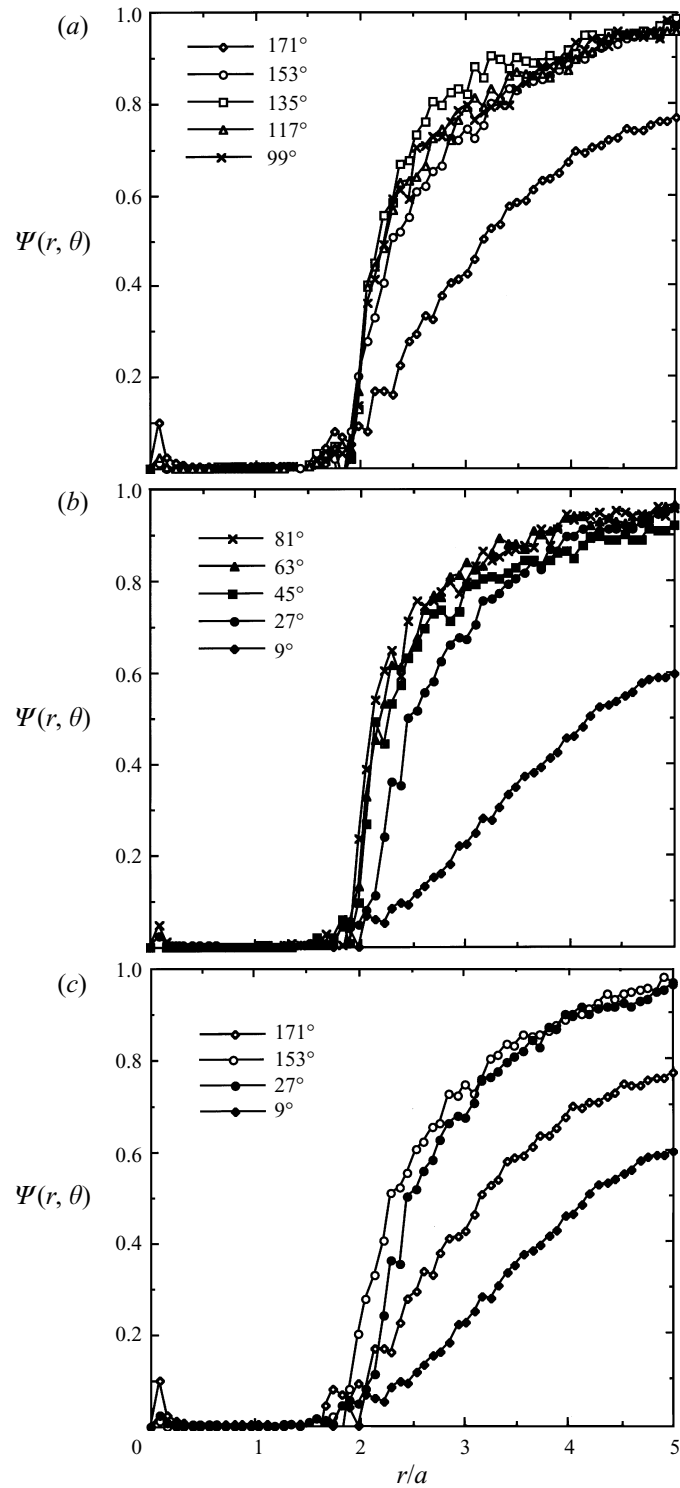
FIGURE 9. Integrated pair distribution function for a 5% suspension: (*a*) the compression quadrant; (*b*) the extensional quadrant; (*c*) close to the flow direction in both the approach and recession quadrants. The sharp reduction in Ψ near the approach ($\theta = 171°$) and recession axes ($\theta = 9°$) indicates a depletion of bound pairs of spheres.

discrete radial and angular positions using the fast fourier transform (FFT) technique to invert the convolution kernel $G(t)$ and then implementing a discrete convolution with $P(t, \theta)$. The inversion process is implemented by first calculating the Fourier transform of the kernel $G(t)$ numerically from the exact analytical expression and then obtaining the inverse of the reciprocal using the FFT technique. The Fourier transform of $G(t)$ was sampled at 4096 points to capture accurately the integrable singularity of the inverse function of $G(t)$ at the origin. The high-frequency noise in $P_a(\tau, \theta)$, inherently associated with this procedure, was filtered out using a three-point low-pass filter, defined as (0.25, 0.5, 0.25). Rampall (1992) describes the procedure used to obtain $P_a(\tau, \theta)$ in more detail.

Figure 8 shows the pair-particle conditional probability distribution function using this deconvolution procedure for experiments with the 10 % suspensions. The experimental and deconvolved radial variation of the pair-particle conditional probability distribution function averaged overall angles in the plane of shear are both shown. The deconvolution procedure significantly reduces the calculated magnitude of the pair-particle conditional probability distribution function in the forbidden region $r/a < 2$. For large r/a, the value approaches the average number density $\phi/(4\pi/3) = 0.0238$ for a 10 % suspension confirming that the correct number and size of particles were successfully identified.

Random errors caused by the finite number of particles in each cell can be suppressed by using the radially averaged PDF, defined as:

$$\Psi(r, \theta_i) = \frac{2}{r^2 \, \Delta\theta} \int_{\theta_i - \Delta\theta/2}^{\theta_i + \frac{1}{2}\Delta\theta/2} \int_0^r q(r, \theta) \, r \, \mathrm{d}r \, \mathrm{d}\theta, \qquad (5.9)$$

where $\theta_i = 9°, 27°, \dots, 171°$. The function Ψ is the normalized average number density of particles in a wedge of radius r having width $\Delta\theta$ of 18° centred at θ_i. Note that Ψ approaches unity as $r \to \infty$. The measured values of Ψ are shown in figures 9–12. Figure 9 shows results for the 5 % suspensions, figures 10 and 11 show results for the 10 % suspensions (from the low- and high-strain subregions, respectively), and figure 12 shows results from the 15 % suspensions. The data in figures 10 and 11 are nearly identical, even though the strain undergone by the suspension leading to the two figures differed by a factor of about four. This provides evidence that the elapsed strain was sufficient for the PDF to approach its steady value. Figures 9(c), 10(c), 11(c) and 12(c) show a depletion of particles in the direction of flow, in agreement with results of Bossis & Brady (1984) (which included repulsive forces), but in contrast to simulation results of Bossis & Brady (1985) (which included only hydrodynamic forces) and experimental measurements of Husband & Gadala-Maria (1987). The distribution is nearly independent of angle for $65° \leqslant \theta \leqslant 135°$. The non-zero values of the PDF near $r = 0$ observed in some of the plots are an artifact of the deconvolution procedure.

Figure 13 shows that the PDF in the 9° wedge increases with increasing concentration; the PDF is consistent with an absence of bound pairs of particles. This increase is probably due to the increased frequency of three-particle interactions at higher concentrations, which leads to the displacement of particles into the closed orbit region.
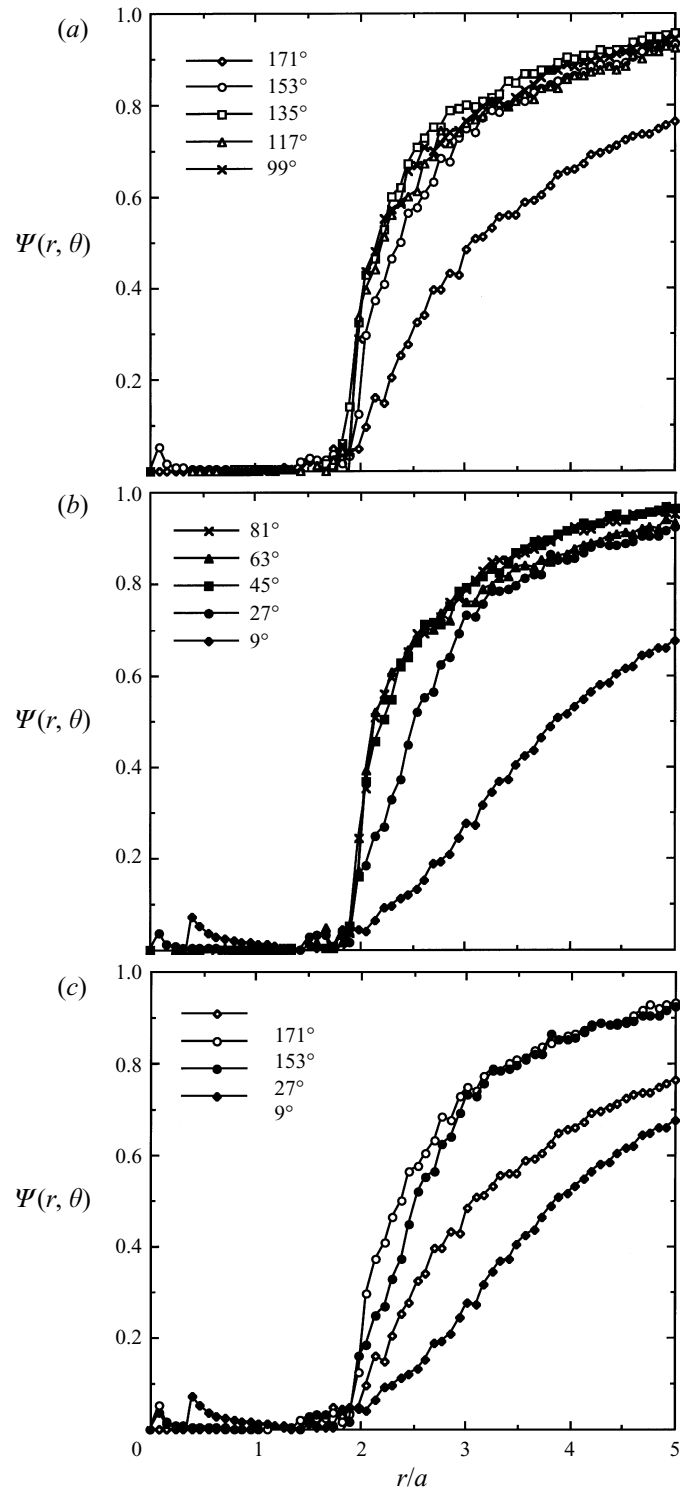
I. Rampall, J. R. Smart and D. T. Leighton

FIGURE 10. Integrated pair distribution function for a 10 % suspension: (*a*) the compression quadrant; (*b*) the extensional quadrant; (*c*) near the approach and recession axes. The results are from the low-strain subregion.
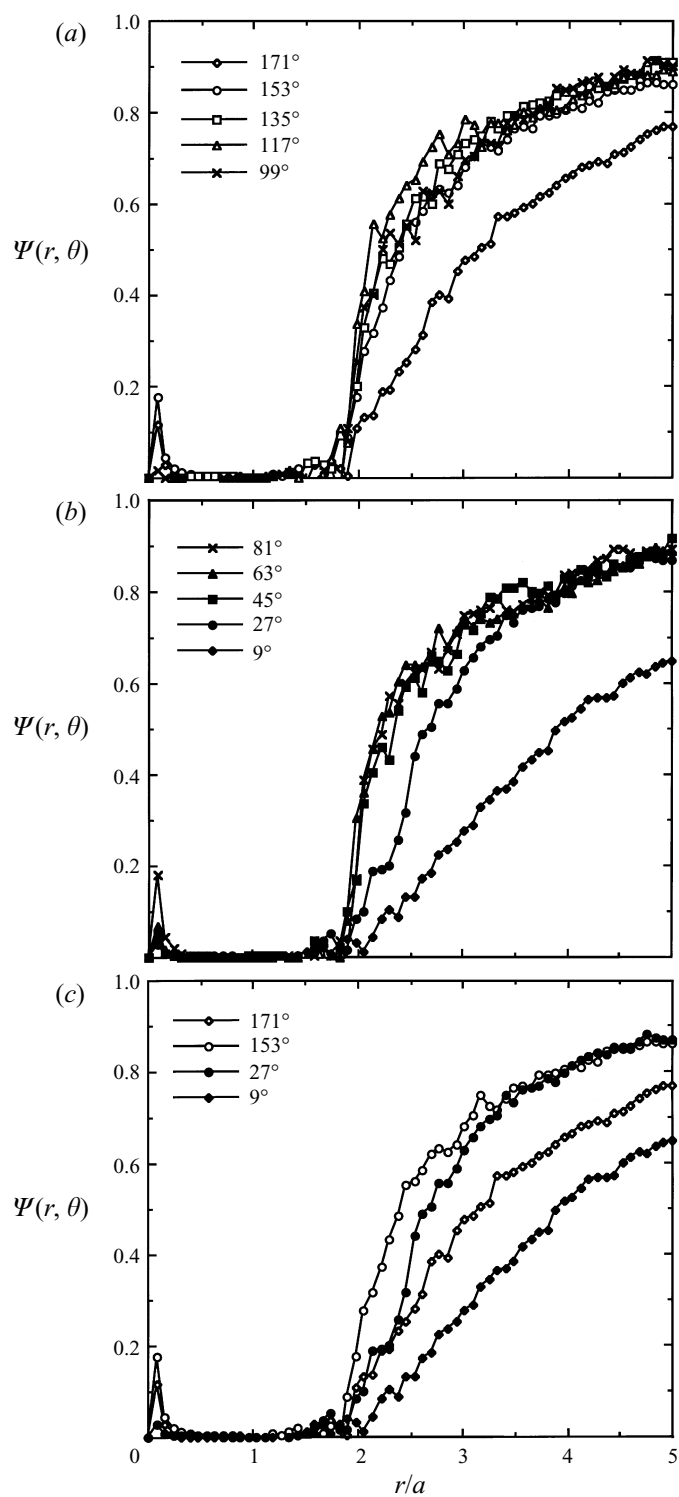
FIGURE 11. Integrated pair distribution function for a 10% suspension: (*a*) the compression quadrant; (*b*) the extensional quadrant; (*c*) near the approach and recession axes. The results are from the high-strain subregion.
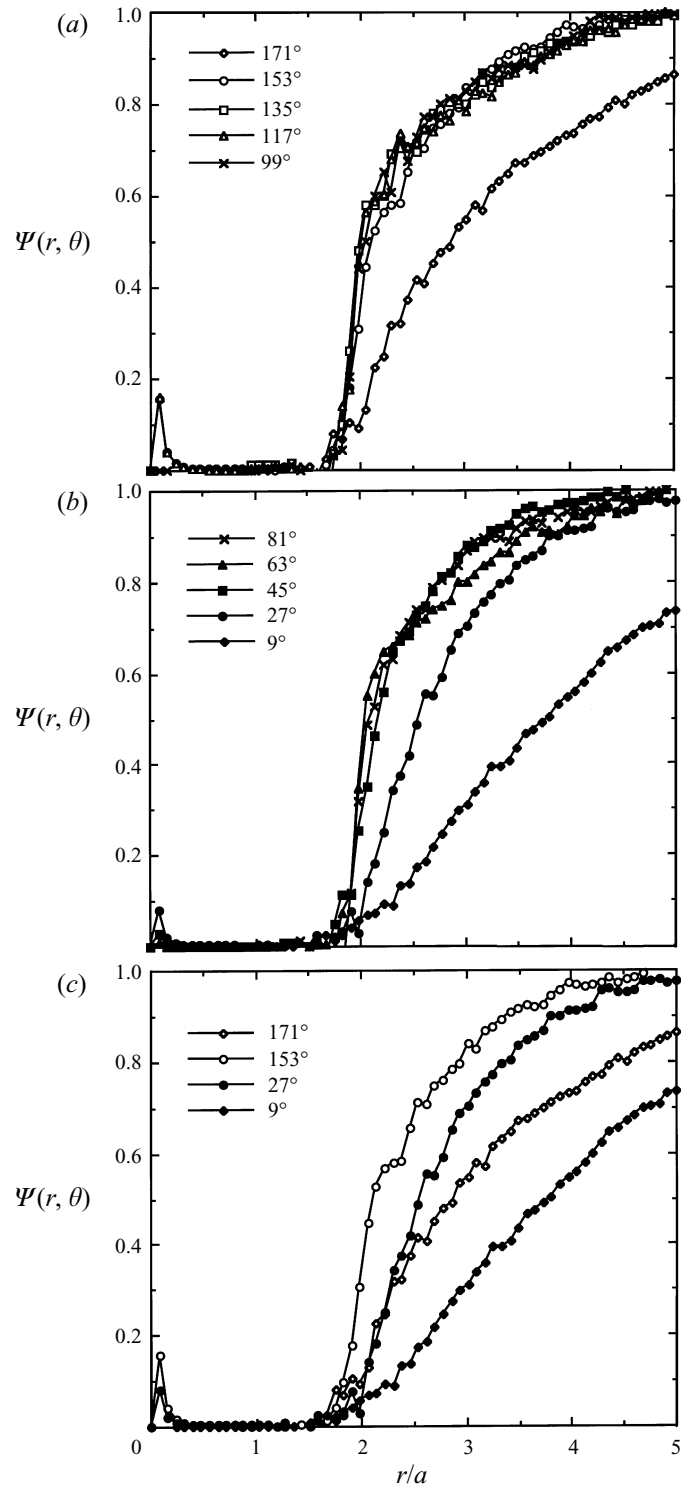
FIGURE 12. Integrated pair distribution function for a 15% suspension: (*a*) the compression quadrant; (*b*) the extensional quadrant; (*c*) near the approach and recession axes. The sharp reduction in Ψ near the approach and recession axes indicates a depletion of bound pairs of spheres.
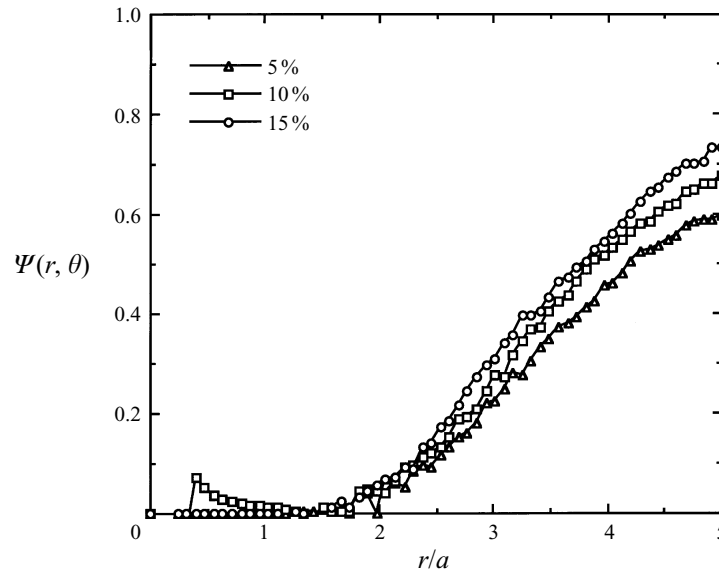
FIGURE 13. Comparison of the depletion of particles in the wedge centred at 9° *vs.* concentration. The depletion of particles is less pronounced at higher concentrations.

6. The influence of roughness on the pair distribution function

Batchelor & Green (1972*a*, *b*) have developed expressions for the motion of one sphere centre relative to another in an arbitrary infinite linear shear flow. From their analysis, Batchelor & Green obtained the pair distribution function in a region outside the closed-orbit region. In this section we modify these equations to include the effects of surface roughness and use them to determine the PDF appropriate for dilute suspensions of rough spheres.

Arp & Mason (1977) calculated that the minimum distance between particle surfaces on the limited closed orbit trajectory of two smooth spheres in the plane of shear of a simple shear flow is about $\epsilon_0 = 4 \times 10^{-5}$ particle radii. The surface roughness (denoted by ϵ_s) of the $\frac{1}{8}$ inch spheres used in the experiments described here was about 4×10^{-3} based on measurements of similar $\frac{1}{4}$ inch PMMA spheres (Smart & Leighton 1989), thus it is likely that closely interacting particles will be strongly influenced by the presence of surface roughness. Indeed, Arp & Mason found that all bound pairs of particles were eliminated by the roughness of their particles.

Kim & Mifflin (1985) and Yoon & Kim (1987) have developed equations to determine the trajectory of one sphere relative to another for two particles suspended in an infinite linear shear flow. Trajectories of smooth spheres interacting in the plane of shear of a simple shear flow can be most easily described with the parameter ϵ_{min}, the minimum gap width between the particles during the interaction. Figure 14 shows two such trajectories with $\epsilon_{min} = 4 \times 10^{-3}$ and 4×10^{-5}. Note that surface roughness is expected to eliminate bound pairs of particles, thus eliminating trajectories lying within the closed orbit streamline, and will modify trajectories lying between the closed orbit and surface roughness streamlines.

To model the effect of roughness on the PDF we shall assume that the roughness simply governs the minimum gap width between particles and has no effect on the hydrodynamic interaction of the particles. A more exact model would combine the interaction due to friction (Smart, Beimfohr & Leighton 1993) with the near-field
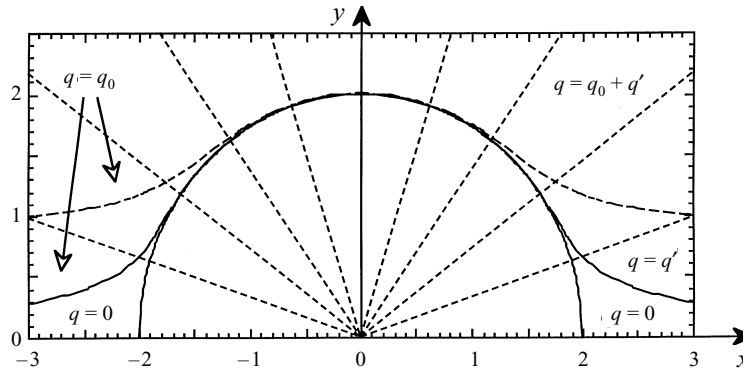
FIGURE 14. Limiting closed orbit and surface roughness trajectories (for $\epsilon_s = 4.0 \times 10^{-3}$) in the plane of shear are shown on the approach and recession sides of the interaction. Note that for interactions outside the plane of shear, the closed orbit trajectory region is enclosed between a surface generated by rotating the closed orbit trajectory curve shown about the y-axis and the (x, z)-plane. The applicable pair distribution function relationships in different regions are also shown.

trajectory equations of Yoon & Kim (1987), but is unlikely to significantly modify the results. Calculations by da Cunha & Hinch (1996) have shown the trajectory of two rough spheres to be virtually identical for the two limiting cases of perfect slip and no-slip between the sphere surfaces.

From our model, if the particle on the approach side of the interaction is on a trajectory such that $\epsilon_{min} < \epsilon_s$, then the particles are forced apart, and the particle leaves on the trajectory whose ϵ_{min} is ϵ_s. It is assumed that roughness does not modify the trajectory of a particle on the approach side of the interaction, and it does not affect the interaction if the particle is on a trajectory such that $\epsilon_{min} > \epsilon_s$ (i.e. in this case the approach and recession parts of the trajectory are identical to those of smooth spheres). The pair distribution function for rough spheres on the approach side of an interaction outside the closed orbit region is thus:

$$q(r, \theta) = q_0(r), \tag{6.1}$$

where $q_0(r)$ is the symmetric pair distribution function derived by Batchelor & Green (1972b), since only hydrodynamic interactions are considered and all trajectories approach from infinity. The PDF inside the closed orbit region is identically zero, since the surface roughness is assumed to be sufficient to eliminate closed trajectories.

On the recession side of an interaction, the pair distribution function for those trajectories which lie outside the surface roughness trajectory (i.e. $\epsilon_{min} \geqslant \epsilon_s$) is

$$q(r, \theta) = q_0(r) + q'(r, \theta), \tag{6.2}$$

and the PDF for particles inside the roughness trajectory (i.e. $\epsilon_{min} < \epsilon_s$) is

$$q(r, \theta) = q'(r, \theta). \tag{6.3}$$

The function $q'(r, \theta)$ represents the contribution to the PDF on the recession side owing to particles between the closed orbit and roughness trajectories which were displaced to the surface roughness trajectory. The regions of validity of these expressions for the PDF are shown in figure 14.

The number of particles displaced by the surface roughness must be determined to
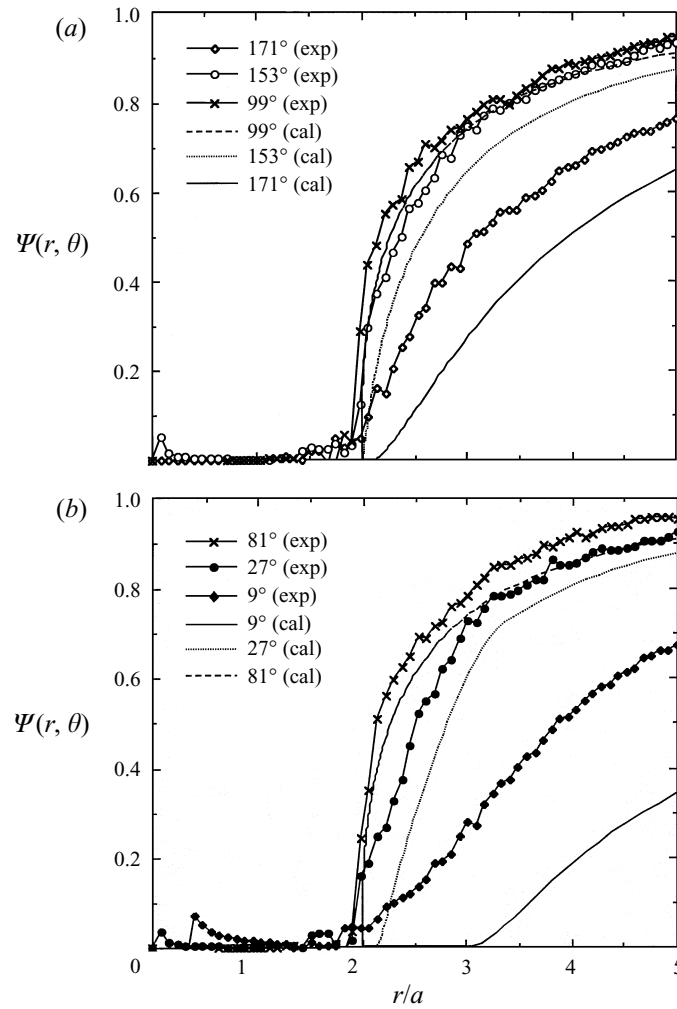
FIGURE 15. Comparison of the experimental and theoretical results (for $\epsilon_s = 4.0 \times 10^{-3}$ and $\sigma = 0.33$) of the pair distribution function: (*a*) the approach quadrant; (*b*) the recession quadrant. Results calculated near the compression and extensional axes are lower than the measurements.

calculate $q'(r, \theta)$. With the assumptions above, this is simply the integral of $q(r)$ from the limiting closed-orbit trajectory to the roughness trajectory:

$$I_{ns} = \int_{2+\epsilon_0}^{2+\epsilon_s} q_0(r)\, dr. \tag{6.4}$$

We shall further assume that these particles are distributed on a range of trajectories about the average surface roughness trajectory, reflecting the observed variance in the surface roughness. Thus,

$$q'(r, \theta) = \frac{q_0(2+\epsilon)}{q_0(2+\epsilon_{min})} I_{ns}\, g(\ln \epsilon_{min} - \ln \epsilon_s), \tag{6.5}$$

where

$$g(\ln \epsilon_{min} - \ln \epsilon_s) = \frac{\exp(-1/2\sigma^2)(\ln \epsilon_{min} - \ln \epsilon_s)^2)}{\epsilon_{min}(2\pi\sigma^2)^{1/2}}. \tag{6.6}$$

We used a Gaussian distribution characterized by the measured standard deviation σ in the logarithm of the surface roughness, which is a good approximation to the shape of the roughness distribution observed by Smart & Leighton (1989).

Calculated values of the radially averaged PDF $\Psi(r, \theta)$ are compared to the 10% experimental results in figure 15. The measured value of absolute roughness and its standard deviation of $\frac{1}{4}$ in. PMMA spheres reported by Smart & Leighton (1989) were used to estimate ϵ_s and σ (4.0×10^{-3} and 0.33, respectively) of the $\frac{1}{8}$ in. PMMA spheres used in the experiments. This assumption is considered to be reasonable since both batches of spheres were supplied by the same manufacturer and made by the same grinding process. The predicted depletion is greater than measured in the regions aligned with the flow ($\theta = 0°, 180°$), however predictions do agree closely with the measurements in the region normal to the flow ($\theta = 90°$). The predicted depletion may be greater than measured because multibody interactions, which force particles into the excluded regions, were not included in the model. While such interactions are unimportant at sufficiently low concentrations, it is not clear whether they can be neglected at the concentrations used in this study. At a concentration of 10%, for example, the average interparticle separation is less than two particle diameters. Most probably, a better quantitative match is possible at much lower concentrations. Nevertheless, the qualitative trends in the measured PDF (particle depletion in regions aligned with the flow and the observed fore and aft asymmetry) provide strong evidence of closed orbit trajectory elimination by surface roughness in two-particle interactions.

7. Conclusions

The observed deficiency of particles on the approach side of the interaction corresponds to a depletion of particles in the closed orbit trajectory region, with spheres approaching from infinity being displaced outside this region. The observed deficiency of particles on the recession side of the interaction is less pronounced than the depletion predicted using the measured magnitude and variance in the surface roughness. While the degree of quantitative mismatch between the experiments and the model is most probably a result of an insufficiently dilute suspension in which multi-body interactions cannot be excluded, qualitative similarities in the results suggest that surface roughness does act to eliminate all bound pairs of spheres in the plane of shear in dilute suspensions.

The predicted and observed anisotropy is qualitatively different from the anisotropy measured in the experiments of Husband & Gadala-Maria (1987). The anisotropy they measured (in a Couette device) corresponds to an excess of bound pairs of particles; the mechanism giving rise to this excess is unclear. Possible explanations may include the slight curvature of the flow field causing the limiting closed-orbit streamline to be greater than the surface roughness, so that roughness is unable to displace particles outside the region of closed trajectories; or there may have been some attractive non-hydrodynamic force present (e.g. van der Waals or some other attractive force). Husband & Gadala-Maria used 50 μm diameter particles in their experiments, and Smart & Leighton (1989) found that this size of particle frequency adhered to a flat plane against the force of gravity. Similar non-hydrodynamic adhesive forces may have caused the excess of bound pairs observed by Husband & Gadala-Maria.

Typical values of the surface roughness for real particles is sufficient to eliminate bound pairs of particles in the plane of shear for dilute suspensions subjected to simple shear flow. Hence the results of Batchelor & Green (1972b) can be used to calculate the

effective viscosity of a suspension to $O(c^2)$ as a function of the surface roughness for monolayer suspensions of spheres. Parker (1986) developed a similar model to find the effect of roughness on the effective viscosity of a suspension. In a fully three-dimensional suspension, however, the problem is much more complex. Batchelor & Green showed that the pair distribution function outside the plane of shear is symmetric with respect to rotation about the y-axis, thus containing the entire zero velocity plane. There exist, therefore, trajectories for which the minimum separation of the closed orbit trajectories lie outside the surface roughness lengthscale, and thus such closed trajectories cannot be eliminated. Theoretical calculations of the viscosity of a fully three-dimensional dilute suspension can only be performed if some assumption is made about the PDF in these closed orbit regions. The calculated viscosity is expected to be insensitive to this assumption, however, as interactions outside of the plane of shear are much weaker than the interactions in the plane of shear.

While a dilute suspension of spheres is strictly Newtonian to $O(c)$, the fore-and-aft asymmetry predicted by our model of surface roughness will lead to normal stress differences at $O(c^2)$. Gadala-Maria (1979) observed this behaviour in concentrated suspensions, but it would be very difficult to measure in dilute suspensions. The structure of the dilute PDF, however, suggests that the asymmetry would lead to the same positive normal stress difference function $v_1 - v_2$ measured for concentrated suspensions.

REFERENCES

ARP, P. A. & MASON, S. G. 1977 Kinetics of flowing dispersions. 9. Doublets of rigid spheres (experimental). *J. Colloid Interface Sci.* **61**, 44.

BATCHELOR, G. K. & GREEN, J. T. 1972*a* The hydrodynamic interaction of two small freely moving spheres in a linear flow field. *J. Fluid Mech.* **56**, 375.

BATCHELOR, G. K. & GREEN, J. T. 1972*b* The determination of the bulk stress in a suspension of spherical particles to order c^2. *J. Fluid Mech.* **56**, 401.

BOSSIS, G. & BRADY, J. F. 1984 Dynamic simulation of sheared suspensions. I. General Method. *J. Chem. Phys.* **80**, 5141.

BOSSIS, G. & BRADY, J. F. 1985 The rheology of concentrated suspensions of spheres in simple shear flow by numerical simulation. *J. Fluid Mech.* **155**, 105.

CUNHA, F. R. DA & HINCH, E. J. 1996 Shear-induced dispersion in a dilute suspension of rough spheres. *J. Fluid Mech.* **309**, 211–223.

EINSTEIN, A. 1906 Eine neue bestimmung der molekuldimensionen. *Ann. Physik.* **19**, 289.

GADALA-MARIA, F. 1979 The rheology of concentrated suspensions. Ph.D. thesis, Stanford University.

GRAHAM, A. L. & BIRD, R. B. 1984 Particle clusters in concentrated suspensions. 1. Experimental observations of particle clusters. *Ind. Engng Chem. Fundam.* **23**, 406.

HO, B. P. & LEAL, L. G. 1974 Inertial migration of rigid spheres in two-dimensional unidirectional flows. *J. Fluid Mech.* **65**, 365–400.

HUSBAND, D. M. & GADALA-MARIA, F. 1987 Anisotropic particle distribution in dilute suspensions of solid spheres. *J. Rheol.* **31**, 725.

KARNIS, A., GOLDSMITH, H. L. & MASON, S. G. 1966 The kinetics of flowing dispersions. 1. Concentrated suspensions of rigid particles. *J. Colloid Interface Sci.* **22**, 531.

KIM, S. & KARRILA, S. J. 1991 *Microhydrodynamics: Principles and Applications*. Butterworth.

KIM, S. & MIFFLIN, R. T. 1985 The resistance and mobility functions of two equal spheres in low Reynolds number flow. *Phys. Fluids* **28**, 2033.

LEIGHTON, D. T. & ACRIVOS, A. 1986 Viscous resuspension. *Chem. Engng Sci.* **41**, 1377.

LEIGHTON, D. T. & ACRIVOS, A. 1987 Shear-induced migration of particles in concentrated suspensions. *J. Fluid Mech.* **181**, 415.

LEIGHTON, D. T. & RAMPALL, I. 1992 Measurement of the shear-induced microstructure of concentrated suspensions of non-colloidal spheres. *Particulate Two-phase Flow*, Chap. 6. Butterworth.

PARKER, A. R. 1986 Particle interactions in fluid suspensions. PhD thesis, University of Cambridge, UK.

PARSI, F. & GADALA-MARIA, F. 1987 Fore and aft asymmetry in a concentrated suspension of solid spheres. *J. Rheol.* **31**, 725.

RAMPALL, I. 1992 Shear-induced structure and migration in non-colloidal suspensions. PhD thesis, University of Notre Dame.

ROSENFELD, A. & KAK, A. C. 1982 *Digital Picture Processing*, vols. 1 and 2. Academic.

SMART, J. R. & LEIGHTON, D. T. 1989 Measurement of the hydrodynamic surface roughness of non-colloidal spheres. *Phys. Fluids A* **1**, 52.

SMART, J. R., BEIMFOHR, S. & LEIGHTON, D. T. 1993 Measurement of the translational and rotational velocities of a non-colloidal sphere rolling down a smooth inclined plane at low Reynolds number. *Phys. Fluids A* **5**, 13.

YOON, B. J. & KIM, S. 1987 Note on the direct calculation of mobility functions for two equal-sized spheres in Stokes flow. *J. Fluid Mech.* **185**, 437.